

# Development of a 10 kHz high harmonic source up to 140 eV photon energy for ultrafast time-, angle-, and phase-resolved photoelectron emission spectroscopy on solid targets

J. Schmidt,<sup>1,a)</sup> A. Guggenmos,<sup>1,2</sup> S. H. Chew,<sup>1,2</sup> A. Gliserin,<sup>1,2</sup> M. Högner,<sup>1,2</sup> M. F. Kling,<sup>1,2</sup> J. Zou,<sup>1</sup> C. Späth,<sup>1</sup> and U. Kleineberg<sup>1,2</sup>

<sup>1</sup>Faculty of Physics, Ludwig-Maximilians-Universität München, 85748 Garching, Germany

<sup>2</sup>Max-Planck-Institut für Quantenoptik, 85748 Garching, Germany

(Received 22 December 2016; accepted 7 June 2017; published online 9 August 2017)

We present a newly developed high harmonic beamline for time-, angle-, and carrier-envelope phase-resolved extreme ultraviolet photoemission spectroscopy on solid targets for the investigation of ultrafast band structure dynamics in the low-fs to sub-fs time regime. The source operates at a repetition rate of 10 kHz and is driven by 5 fs few-cycle near-infrared laser pulses generating high harmonic radiation with photon energies up to 120 eV at a feasible flux. The experimental end station consists of a complementary combination of photoelectron detectors which are able to spectroscopically address electron dynamics both in real and in k-space. The versatility of the source is completed by a phase-meter which allows for tracking the carrier-envelope phase for each pulse and which is synchronized to the photoelectron detectors, thus enabling phase sensitive measurements on the one hand and the selection of single attosecond pulses for ultimate time resolution in pump-probe experiments on the other hand. We demonstrate the applicability of the source by an angle- and carrier-envelope phase-resolved photoemission measurement on a tungsten (110) surface with 95 eV extreme ultraviolet radiation. *Published by AIP Publishing.* [<http://dx.doi.org/10.1063/1.4989399>]

## I. INTRODUCTION

High harmonic generation (HHG) has enabled the development of broadband and coherent radiation sources from the extreme ultraviolet (EUV) energy range up to the soft X-ray region at a table-top size. It also forms the basis for the generation of attosecond pulses<sup>1</sup> which allows for studying electron dynamics with ultimate time resolution.<sup>2,3</sup> Due to these unique characteristics, it has become an inevitable tool in numerous applications such as ultrafast time-resolved photoelectron spectroscopy (PES),<sup>4,5</sup> EUV microscopy,<sup>6</sup> and interferometry and diffraction experiments.<sup>7</sup> All of them require specially tailored harmonic radiation. The advance of high harmonic radiation is closely related to laser development, with the objective to precisely shape the laser pulses which drive the harmonic process on the one hand and to the development of advanced EUV optics<sup>8</sup> on the other hand. The refinement of laser pulse compression techniques has enabled the generation of ultrashort few-cycle pulses, which are advantageous for the HHG process. They produce a broadband EUV continuum at the harmonic cutoff from which, with the appropriate optics, almost any required spectral content regarding central photon energy, bandwidth, and chirp can be extracted. The success of few-cycle pulses is also attributed to the development of techniques which allow the control of the carrier-envelope phase (CEP) of these pulses by means of both its stabilization<sup>9–11</sup> and its single-shot measurement for CEP tracking.<sup>12,13</sup> CEP control not only gives further insight into the high harmonic generation process itself but also has paved the way for

the investigation of phase effects in other processes such as charge migration,<sup>14</sup> multiphoton ionization,<sup>15</sup> and strong-field interaction.<sup>16</sup>

The most practical and common way of generating high harmonic radiation is by the interaction of intense laser pulses with a gas target according to the HHG three step model.<sup>17</sup> This technique typically requires laser intensities in the  $10^{14}$ – $10^{15}$  W/cm<sup>2</sup> range. Predominantly ultrashort near-infrared (NIR) laser pulses are employed for this purpose. Key parameters in the design of a HHG source are the repetition rate, high harmonic cutoff energy,<sup>18,19</sup> and yield.<sup>20</sup> The simultaneous realization of these requirements is intricate due to various difficulties in the specific laser amplifier or cavity design. Especially photoemission experiments benefit from a high repetition rate whereas the usable yield is usually limited by space charge effects. Additionally, it is desirable to have a high cutoff energy which allows the access of electronic states of different binding levels.<sup>21</sup> Currently, most few-cycle driven high harmonic sources which provide photon energies beyond 100 eV with suitable flux for EUV spectroscopy or imaging are based on regenerative or multi-pass amplifiers with repetition rates of 1–3 kHz.<sup>22–24</sup> However, ongoing effort is put into the development of high harmonic sources which boost the repetition rate to multi-hundred kHz<sup>25,26</sup> or even MHz<sup>27,28</sup> but at the cost of a (greatly) reduced cutoff energy or harmonic yield. Although the harmonic output has been demonstrated from these sources, many of them still lack proof of their applicability to experiments. Also, pulse compression down to the few-cycle regime for CEP sensitive measurements has not yet been shown with MHz rate harmonic sources. The high harmonic source we present here provides a reasonable balance between repetition rate and cutoff energy. It is based on the

<sup>a)</sup>Electronic mail: juergen.schmidt@physik.uni-muenchen.de

proven multi-pass amplifier design but with an increased repetition rate of 10 kHz which is able to deliver a high harmonic cutoff energy well beyond 100 eV. The source employs few-cycle NIR pulses to drive the HHG process. Owing to their steep rise in intensity, they promote the generation of high-energy harmonics near the cutoff at reasonable yields due to low fractional ionization levels, i.e., a significant fraction of gas atoms remain neutral (non-ionized) until the highest field amplitude of the driving laser pulse reaches the interaction zone. Additionally, few-cycle pulses are a prerequisite for the generation of isolated attosecond pulses using amplitude gating or other gating techniques.<sup>29</sup> This provides ultimate time resolution in pump-probe experiments. The CEP of the few-cycle pulses is continuously tracked for every laser shot by a stereo above-threshold-ionization (ATI) phase-meter<sup>30</sup> which is synchronized to the electron detector for photoemission spectroscopy measurements. As the laser source itself is not actively phase stabilized, the CEP of the NIR pulses changes randomly at every laser shot, thus intrinsically covering the full  $360^\circ$  range, which is ideal for CEP related studies. The high harmonic output can be adapted to the needs of various applications by means of home-made tailored, multilayer-based EUV optics.<sup>31–33</sup> Furthermore, the polarization state of the EUV radiation can be changed to nearly circular polarization by the use of EUV phase shifters.<sup>34</sup> The experimental end station comprises an electron detector for angle-resolved photoemission spectroscopy (ARPES) as well as a photoemission electron microscope (PEEM).<sup>35</sup> The combination of these complementary detection techniques enables to spectroscopically investigate electron dynamics both in real and in reciprocal space. The performance of the PEEM at a high harmonic source of 1 kHz repetition rate is described elsewhere.<sup>36</sup> Here we present as a proof-of-principle application a CEP-resolved ARPES measurement on a tungsten (110) surface at 95 eV photon energy.

## II. EXPERIMENTAL

### A. Laser front-end

The laser front-end of the beamline is designed to provide ultrashort few-cycle pulses with a carrier wavelength of 730 nm and  $\sim 100 \mu\text{J}$  pulse energy at a repetition rate of 10 kHz. It consists of a commercial femtosecond laser source, an additional nonlinear pulse compression setup in conjunction with dispersion management, as well as a single-shot phase-meter for CEP tracking. The laser source is a Ti:sapphire multi-pass chirped pulse amplification (CPA) system (Femtower Compact Pro, Femtolasers GmbH) delivering pulses of 400  $\mu\text{J}$  energy and 25 fs full width at half maximum (FWHM) duration centered at 780 nm at 10 kHz repetition rate. The increased repetition rate comes at the expense of a reduced pulse energy compared to systems of lower rates. As gain narrowing limits the effective spectral bandwidth transmitted through the amplifier system, the spectrum is externally broadened by the nonlinear process of self-phase-modulation (SPM) in a gas medium for further compression. The gas is filled into a hollow-core fiber (HCF) which guides the laser focus over a sufficiently long distance to build up the desired spectral

content. Adjusting the gas pressure in the capillary conveniently allows the control of the magnitude of nonlinearity for the SPM process. Argon is chosen as the gas medium because of its sufficiently strong nonlinearity for the applied pulse energies. In this way, the gas pressure can be kept at practical values around 1 bar. However, ionization losses reduce the total fiber throughput to 40%, even for a coupling condition close to the theoretical optimum.<sup>37</sup> The fiber is made of fused silica and is 1 m long with a core diameter of 300  $\mu\text{m}$ . Since spatiotemporal pulse distortions as well as beam pointing instabilities and drifts heavily degrade the coupling efficiency, an acousto-optic programmable dispersion filter is installed before the fiber for optimizing the spectral shape and the dispersion of the input pulses, along with an active beam stabilization setup. The latter significantly improves the long-time stability of the system.

Figure 1 shows the pulse spectra right before and after the fiber for an argon pressure of 900 mbar.

A spectral broadening factor of  $F = 7.5$  is achieved with only a moderate gas pressure, resulting in a spectrum spanning more than one octave from 450 nm to over 950 nm.  $F$  is defined as  $F = \Delta\lambda_{\text{after}}/\Delta\lambda_{\text{before}}$  with  $\Delta\lambda^2 = \langle(\lambda - \lambda_0)^2\rangle - \langle(\lambda - \lambda_0)\rangle^2$ , where  $\lambda_0$  is the central wavelength and the angle brackets denote the spectral average over the wavelength  $\lambda$ . Finally, the chirp is removed by eight consecutive reflections on four balanced pairs of low-ripple negative group delay dispersion (GDD) dielectric mirrors.<sup>38</sup> They support a bandwidth from 500 nm to 1050 nm and are optimized for highest reflectivity, giving an overall throughput of the entire mirror compressor of better than 94%. The theoretical spectral transmission characteristic is also shown in Fig. 1(a) (blue line). Dispersion fine tuning is done by a pair of thin glass wedges. The temporal phase and intensity structure of the pulse after

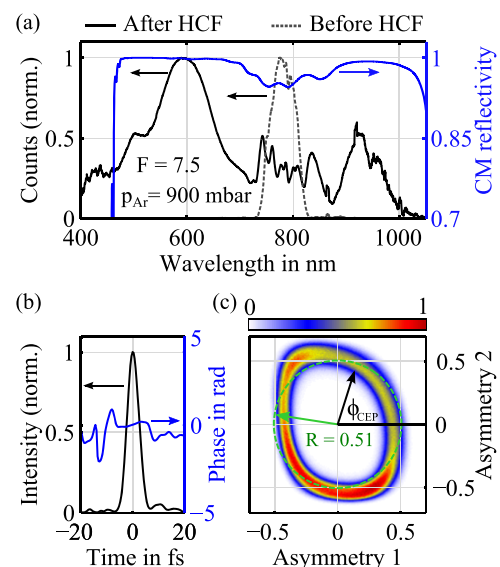


FIG. 1. (a) Laser spectra before and after the SPM process in the HCF. The capillary is filled with argon at a pressure of 900 mbar. The spectrum is broadened by a factor of  $F = 7.5$ . The simulated overall reflectivity characteristic of the chirped mirror (CM) compressor is also shown. (b) Reconstructed temporal phase and pulse shape using a frequency-resolved optical gating (FROG) device. The retrieved pulse duration is 5.3 fs FWHM. (c) Measured PAP for  $41 \times 10^6$  consecutive laser shots. The color bar indicates the normalized counts.

compression is determined by a frequency-resolved optical gating (FROG) device using a four-wave mixing process as nonlinearity in a 70  $\mu\text{m}$  thin glass slab made of AF 32@ eco (Schott AG). The reconstructed pulse structure is depicted in Fig. 1(b), indicating a pulse duration of 5.3 fs FWHM. Before the beam is fed into the vacuum system for HHG and to the experiment, 30% of its energy is extracted by a beam splitter and directed to the stereo ATI phase-meter. The device is capable of measuring the CEP and pulse duration of individual few-cycle laser pulses simultaneously by exploiting the CEP-dependent asymmetry in the ATI spectra from a photo-ionized gas target recorded at opposite sides along the polarization axis of the laser pulse. For each of both spectra, an asymmetry parameter between an integrated low-energy and high-energy part is derived.<sup>13</sup> In this way, one pair of asymmetry parameters is obtained for each laser shot. It is customary to visualize the asymmetry parameters of all recorded laser shots as a two-dimensional histogram with the axes representing the respective asymmetry values. This is referred to as a parametric asymmetry plot (PAP) with the CEP value being the plot parameter. Provided the asymmetry parameters were properly defined,<sup>30</sup> this forms a nearly circular distribution of counts where each count represents a laser shot within its respective bin of asymmetry values. The CEP of a laser pulse is given by the polar angle of its corresponding count in the PAP, while the distance to the origin encodes its pulse duration. The relation between the mean radius of the count distribution in the PAP and the mean pulse duration was empirically found to be<sup>39</sup>

$$\Delta\tau = \beta + \sqrt{(-\alpha / \ln(1 - r))}, \quad (1)$$

where  $\alpha = 9.7317 \pm 1.5069$  and  $\beta = 1.6063 \pm 0.2593$ . A measured PAP for  $41 \times 10^6$  consecutive laser shots is shown in Fig. 1(c). The mean radius of the point distribution is obtained to be 0.51, which yields, after applying Eq. (1), a mean pulse duration of 5.3 fs and precisely confirms the result of the FROG measurement.

## B. Vacuum back-end

The vacuum part of the beamline contains the setup for the generation of the high harmonic radiation, its spectral shaping and characterization as well as the experimental end stations. A sketch of the entire setup is depicted in Fig. 2.

For the HHG process, we use a free gas jet configuration because of its simple implementation. In this scheme, the laser pulse is focused onto a gas jet of noble gas which continuously streams through a small orifice of a nozzle into the vacuum chamber. The nozzle consists of a thin-walled stainless steel tube whose upper end is sealed. The laser pulses pass the tube through two small apertures along the beam axis. The pulse energy at the nozzle position is typically around 80  $\mu\text{J}$ . In order to achieve the required intensity for HHG of  $10^{14}$ – $10^{15}$  W/cm<sup>2</sup> in the gas plume, focal lengths between 30 cm and 40 cm are used. Due to the given Rayleigh length for this focusing condition, which in turn affects the effective coherence length for the harmonics to build up constructively, the nozzle thickness along the beam direction is usually below 1 mm in order to achieve the strongest harmonic output. The nozzle is movable in three dimensions to precisely adjust its orifice to the laser beam. The harmonic output is optimized by the common “knobs” for affecting the phase matching<sup>40</sup> of the conversion process: nozzle position along the beam axis relative to the focus, backing pressure of the gas jet, laser pulse chirp (glass wedges), and pulse intensity (adjusted by an iris). Adjusting these parameters allows, within certain limits, for a spectrally selective enhancement of the harmonic yield. Furthermore, the polarization state of the harmonic radiation can be adapted to different experimental requirements. It can be switched between horizontal and vertical linear polarization by switching between two beam paths, which either feed the fundamental beam via a parallel or via a crossed periscope into the vacuum chamber. This scheme does not degrade the polarization’s degree of linearity for the spectrally broadband NIR pulses, as opposed to inherently narrow-band NIR wave

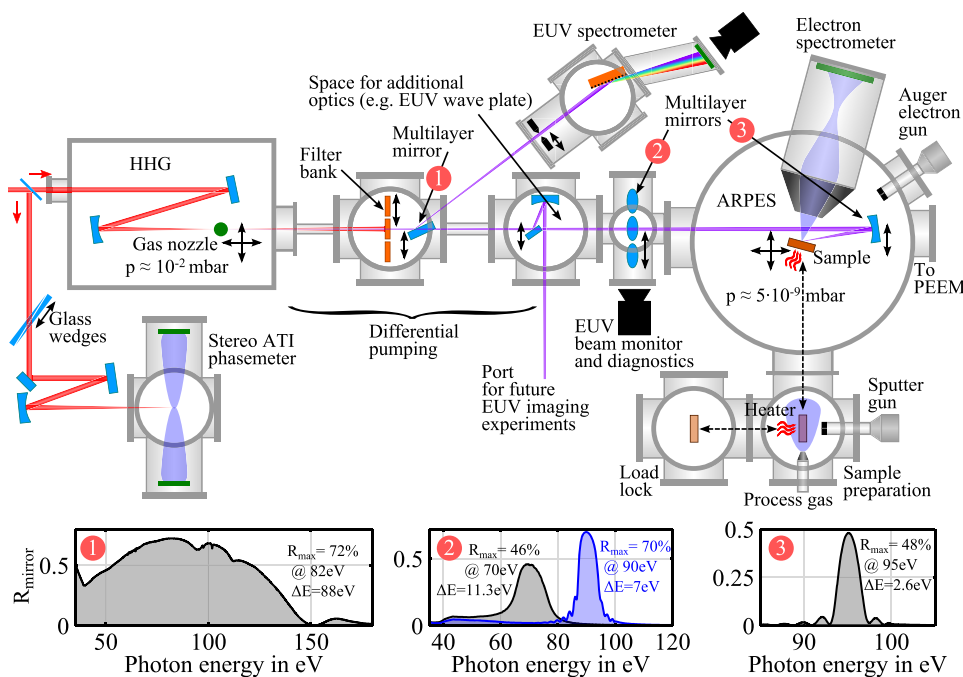


FIG. 2. Schematic of the vacuum back-end of the beamline including the setup for HHG, EUV beam monitoring and diagnostics as well as its spectral shaping and characterization, the setup for CEP tracking, and the experimental chamber together with the setup for sample preparation and handling. The three graphs at the bottom show the reflectivity characteristics of the multilayer mirrors.

plates, which is essential for an efficient HHG conversion from gas targets.<sup>41</sup> Additionally, the linear polarization state of the harmonics can be transformed into elliptical polarization with a high degree of ellipticity by means of broadband EUV quarter-wave plates,<sup>34</sup> which can be installed downstream in the beamline.

It turned out that thermal effects induced by peripheral beam parts striking the edge of the nozzle orifice lead to considerable instabilities and a drop of the harmonic yield within an experimental acquisition cycle. In order to reduce those instabilities and to achieve suitable long-term stability of the harmonic output, the apertures of the nozzle are machine-drilled to about three times the  $1/e$  diameter of the NIR beam at the focus and, additionally, the pointing of the beam is actively stabilized before the nozzle. Moreover, as the HHG chamber is situated on the optical table, it is vibrationally decoupled from the latter while the breadboard inside the chamber which holds the nozzle setup and further optics is firmly attached to the optical table. In this way, the transmission of vibrations from the vacuum pumps to the optical setup is minimized.

After the HHG process, both the residual fundamental NIR and the harmonic EUV beam propagate collinearly, but with different divergence, towards the experimental chambers, thereby passing a differential pumping section with two intermediate chambers in between. This section bridges the pressure difference between the HHG chamber with high gas load at typically  $10^{-2}$  mbar and the experimental chamber at UHV conditions in the low  $10^{-9}$  mbar range. Each chamber is pumped by a turbo pump with a nominal pumping speed of 600 l/s. Clean UHV conditions in the experimental end section are a prerequisite for photoemission experiments on solid targets. The intermediate chambers serve as auxiliary pumping points within the pressure gradient and provide additional ports for EUV filters and optics. Differential pumping is supported by introducing a high gas flow resistance between the chambers via narrow vacuum tubes which additionally contain a set of round apertures. The number and size of the apertures as well as the pumping speed of the vacuum pumps were optimized by simulations so that spatial dimensions are kept in a practical range while maintaining the desired pressure difference at the same time. The apertures can be easily exchanged to meet altered requirements if necessary, e.g., when a different focusing condition changes the beam divergence. This configuration provides a free-space connection between the high harmonic and the experimental chambers, which ensures the highest transmission and flexibility regarding the use of additional optical elements such as different types of EUV filters. If necessary, the vacuum condition in the experimental chamber can be further improved by physically separating it from the HHG chamber by means of a gate valve with an appropriate EUV filter inset. The first intermediate chamber contains a broadband lanthanum/molybdenum multilayer mirror at  $15^\circ$  grazing incidence which reflects the harmonic beam into an EUV spectrometer for spectral diagnostics. The spectrometer employs an aberration-corrected varied line-space flat-field grating (Hitachi High Technologies America, Inc.) and a multichannel plate with phosphor screen as a detector. An input slit with adjustable width allows the adaption either for high throughput or high resolution. A set of ultrathin aluminum,

zirconium, carbon, and silicon foils is used to (a) block the NIR beam, (b) to spectrally filter the harmonic radiation, and (c) for calibrating the spectrometer. The second intermediate chamber serves as a selector for different experimental end stations and provides space for additional optics such as EUV wave plates. EUV multilayer mirrors can optionally feed the harmonic beam into another experimental setup for future applications on EUV diffraction imaging. Moreover, an EUV beam monitoring system is installed in front of the main experimental chambers. A set of retractable multilayer mirrors reflect the harmonic beam onto an EUV sensitive CCD chip. The mirrors are designed for three distinct, adjacent spectral regions between 50 and 90 eV. Hence, this setup provides a quick and easy way to optimize both the harmonic beam profile and yield in a spectral region which can be chosen close to the photon energy of interest for the photoemission experiment.

Finally, the experimental end station consists of two cascaded chambers dedicated to the (micro-)spectroscopic investigation of electron dynamics with sub-fs time resolution in solids using photoemission. The first chamber is equipped with an angle-resolving time-of-flight (TOF) electron spectrometer (Themis 1000, Specs Surface Nano Analysis GmbH) for time-resolved band structure analysis (tr-ARPES) and Fermi surface imaging, while the second chamber houses a TOF photoemission electron microscope (TOF-PEEM, Focus GmbH) for the investigation of electron dynamics on nano-structured samples. The ARPES spectrometer images the emission angles of the photoelectrons via a set of electrostatic lenses onto the detector. Different lens settings allow the adjustment of the acceptance angle and the energy window for the imaging process. The detector is a multichannel plate with a delay-line anode which is able to simultaneously measure the TOF and the position for every electron event.<sup>42</sup> The EUV beam is focused by a multilayer mirror with a focal length of 12.5 cm and at a grazing angle of  $30^\circ$  onto the sample. This mirror is concentrically split where the inner part is mounted on a precise piezo table to adjust nanometer-sized displacements, thus providing the capability to conduct time-resolved EUV-NIR pump-probe experiments with sub-fs time resolution. It can be retracted from the beam axis to let the beam alternatively pass to the second experimental chamber. The ARPES chamber also contains an electron gun for Auger spectroscopy in order to check the surface cleanliness of the sample. The sample manipulator can hold several samples in parallel and is built up by a linear 2-axes translation table allowing both the precise adjustment of the working distance and the selection of the sample. Additionally, the sample can be heated up to a temperature of  $1700^\circ\text{C}$  by electron bombardment. In this way, ARPES measurements can be performed at room temperature and above. The heater is also useful to quickly clean the surface of refractory materials between acquisition cycles. The chamber body is embedded into a triaxial coil setup which is able to compensate for static magnetic stray fields, predominantly the earth's magnetic field. The remanent magnetic field within the volume of interest is kept in this way below  $2\ \mu\text{T}$  resulting in a maximum angle error of  $0.2^\circ$  for 90 eV electrons. For this purpose, the chamber and its ports are made of a stainless steel alloy with reduced magnetic permeability. In addition, it is connected to a sample preparation and loading station for

fast and convenient sample transfer. The sample preparation chamber is equipped with an ion-gun for sputtering the sample surface, a gas port for flushing it with different process gases, and a heater which is able to heat the sample above 2000 °C. The entire sample preparation and loading section can flexibly be moved and attached to either of the experimental chambers.

### III. RESULTS AND DISCUSSION

#### A. High harmonic output

High harmonic radiation is generated in neon with a focal length of 40 cm, giving an intensity of  $\sim 10^{15}$  W/cm<sup>2</sup> in the focal plane at a pulse duration of 5 fs. The nozzle is placed slightly in front of the focus position and has a thickness of 900  $\mu$ m along the beam axis. The harmonic yield in dependence of the backing pressure is shown in Fig. 3. The spectra are taken at a pressure step of 20 mbar; however, for a smoother presentation, they are interpolated to a step width of 5 mbar. Optimum phase matching in the cutoff region is achieved at a backing pressure of 200 mbar. The cutoff energy is around 140 eV. For lower photon energies ( $<70$  eV), the pressure for best phase matching shifts to higher values.

The spectrum shows the typical structure of distinct harmonic peaks in the low energy range which transform into a continuum at the cutoff region as it is common for few-cycle driven HHG.<sup>43</sup> Isolated attosecond pulses can be generated by filtering the spectral continuum where the pulse duration is ultimately limited by the spectral width of the continuum and, in particular, determined by the width of the employed EUV bandpass filter as well as the overall chirp characteristics. The upper panels indicate the transmission characteristics of the employed metal filters and multilayer optics. The flux at 90 eV within a bandwidth of 8% is estimated to be  $5 \times 10^9$  photons/s. The value is derived from the integrated beam profile measured with the 90 eV mirror (reflectivity: 70%, bandwidth: 7 eV) at the high harmonic beam monitoring and diagnostics unit considering the transmission of the involved EUV optics and the quantum efficiency of the EUV CCD for the given energy range.

#### B. CEP- and angle-resolved PES

The following PES measurements were carried out with a molybdenum-silicon multilayer focusing mirror acting as a spectral bandpass filter centered at 95 eV with a bandwidth of

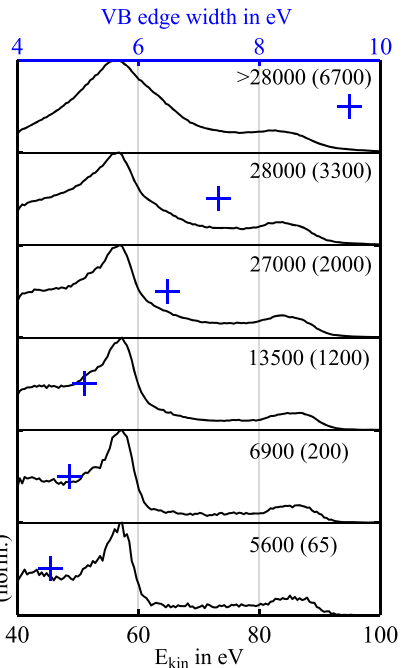
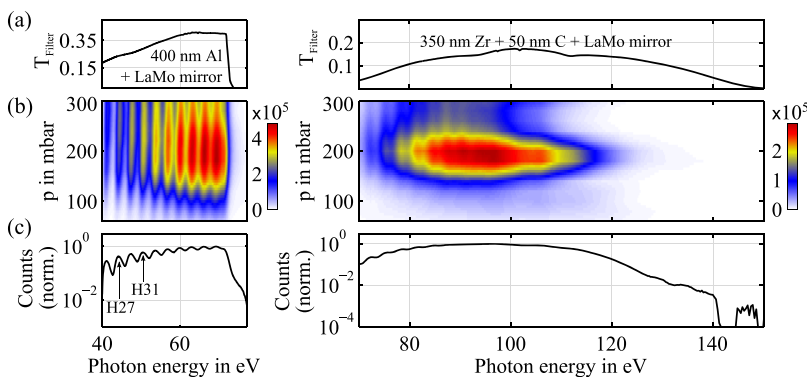


FIG. 4. Degradation of photoemission energy spectra from tungsten (110) by space charge at 95 eV excitation energy. With increasing intensity, the spectral features broaden and smear out. The width (10%–90% criterion) of the high energy edge of the valence band is additionally shown as a quantitative measure (blue crosses). The value attached to each curve indicates the total electron count rate on the detector (including secondary electrons) as well as, in parentheses, the effective electron count rate considering only the electrons within the kinetic energy window adjusted by the spectrometer's lens settings.

2.6 eV and a peak reflectivity of 48%. The bandwidth of the mirror supports Fourier-limited pulses of 700 as FWHM pulse duration for sub-fs time resolution in time-resolved experiments. The angle- and CEP-integrated PES spectra from a tungsten (110) surface are depicted for different harmonic intensities within the mirror bandwidth in Fig. 4. The lower panel in the figure shows the principal structure of the spectrum. Due to the broad excitation bandwidth, the fine structure of the valence band (VB) and the spin-orbit splitting of the 4f core state merge into two prominent peaks at around 90 eV and 58 eV, respectively (work function  $\sim 5$  eV). The collection angle of the spectrometer is adjusted to  $\pm 7^\circ$ . It is evident from this measurement that the spectral shape experiences space charge deformation with increasing harmonic intensity, which manifests in severe broadening and spectral shifting of the peaks.

FIG. 3. High harmonic spectra generated in neon. (a) Filter and multilayer mirror transmission. (b) Spectra at different gas pressures indicating the pressure dependent phase-matching behavior. The color bars indicate the detector counts. (c) Logarithmic plot of the spectrum at 200 mbar (highest signal strength near cutoff, counts are normalized). Cutoff: 140 eV.

Note that the effective electron count rate on the detector for an undistorted image, i.e., the counts of those electrons which fall into the energetic window imaged by the spectrometer, may become very low and may make up only a small fraction of the pulse repetition rate. This demonstrates the limitation of the usable flux and underlines the importance of a source with an increased repetition rate. Furthermore, driving the photoemission signal into the space charge limit indicates that the high harmonic flux generated by this source is sufficient to fully exploit its potential regarding the repetition rate and hence, to efficiently conduct photoemission spectroscopy measurements. Note that for a given photoelectron rate, space charge contributions can be slightly reduced by lowering the number density of photoelectrons in the excitation zone. Therefore, the sample is positioned a few millimeters off the beam waist position in the following measurements in order to increase the excitation area. Considering the actual EUV beam parameters, a theoretical beam waist diameter of nearly  $3 \mu\text{m}$  is calculated after the focusing mirror. The actual beam diameter on the sample, however, is in the order of hundreds of micrometers, e.g., a FWHM diameter of  $270/490 \mu\text{m}$  has been estimated for the short/long axis of the sample spot in a previous measurement, yet with a slightly different longitudinal sample position, using the spatial imaging mode of the Themis analyzer.

The tungsten surface is cleaned in the attached sample preparation chamber by annealing it at  $1000 \text{ }^\circ\text{C}$  in an oxygen atmosphere with a partial pressure of  $1 \times 10^{-7}$  mbar to remove carbon followed by high temperature flashes above  $2000 \text{ }^\circ\text{C}$  in order to desorb the oxygen and the oxide layer.<sup>44</sup> Between subsequent measurement cycles, the sample can be exposed to high temperature power flashes by the *in situ* heater in the main chamber to remove adsorbent gradually grown from the residual gas atmosphere.

For the following measurements, the angle acceptance of the spectrometer is increased to the maximum value of  $\pm 15^\circ$  in order to image the largest k-space possible with the given excitation energy. The kinetic energy window of the lenses for the angle imaging is adjusted to the valence band. Figure 5 shows the characterization of the spectrometer in this mode with respect to kinetic energy and emission angle. The width of the high energy slope of the valence band in the photoemission spectrum is determined to be  $3.5 \text{ eV}$ , based on a 10%–90% criterion. Deconvolving the employed mirror bandwidth by quadratic subtraction results in an instrumental energy resolution of  $2.3 \text{ eV}$ . The energy resolution is potentially limited by space charge contributions and the time resolution of the delay-line detector which has been measured to  $420 \text{ ps}$ . Considering the time-energy dispersion of the photoelectrons, excited by  $95 \text{ eV}$  photon energy from a point-like excitation spot, inside the drift tube of the spectrometer according to the specific lens settings, raytracing simulations indicate an expected energy resolution of  $1.2 \text{ eV}$  based on the given time resolution of the delay-line. The deviation to the experimental value is attributed to remanent space charge and a finite size of the excitation spot. The effective, accumulated spot size is finally determined by including pointing fluctuations which are roughly estimated to make up 40% of the actual spot size diameter. Note that the time resolution of the delay-line detector only affects the

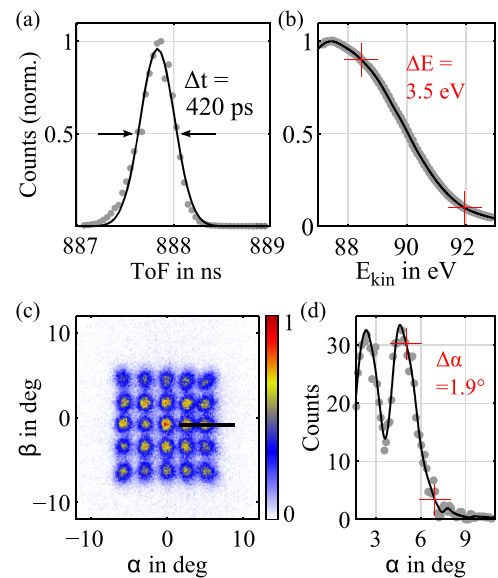


FIG. 5. Characterization of the electron spectrometer. (a) Light peak on the delay-line detector obtained by diffusely reflected high harmonic radiation from the sample. The indicated FWHM is a measure for the system's time resolution. (b) Width of the Fermi edge (10%–90% criterion) in wide-angle mode ( $15^\circ$  acceptance angle) at  $95 \text{ eV}$  photo-excitation. (c) Angle image obtained with a hole pattern aperture as an angle filter from scattered electrons on the sample. The color bar indicates the normalized detector counts. (d) Lineout from (c) as indicated by the black line.

energy resolution of the spectrometer. It is not directly related to the time resolution of pump-probe measurements which is limited by the pulse duration of the probe pulse.

In order to determine the angle imaging quality for the given parameters, an aperture with a square  $5 \times 5$  hole pattern acting as an angle filter is placed between the sample and the inlet of the spectrometer ( $22 \text{ mm}$  distance to the sample). The diameter of the holes is  $300 \mu\text{m}$  and the spacing between them is  $1 \text{ mm}$ . As the aperture blocks the beam path of the harmonic radiation to the multilayer mirror, the electron gun is used as an excitation source. The electron beam is focused onto the sample at an incident angle of  $45^\circ$ , and the inelastically scattered electrons are imaged by the spectrometer. The recorded angle pattern is depicted in Fig. 5(b). It has to be noted that the electron gun produces a rather broad illumination spot on the sample, which is considerably larger than that from the excitation with EUV radiation and which induces slight distortions in the imaging process. An angle resolution of  $1.9^\circ$  is deduced from the edge steepness of the lineout in Fig. 5(c) by a 10%–90% criterion, which however can be considered as an upper limit due to the large illumination spot size.

As an exemplary angle-resolved photoemission measurement using EUV high harmonic radiation at  $95 \text{ eV}$ , a broadband k-space image of the valence band around the Fermi energy is acquired and depicted in Fig. 6, indicating the symmetry structure of the lattice. The projection of a calculated Fermi surface of tungsten using the linear muffin tin method is also shown for comparison. An energy slice with a width of  $200 \text{ meV}$  at the Fermi edge is used for this calculation.

Finally, we present a CEP-resolved PES measurement of the valence band from tungsten. As the detector events in the

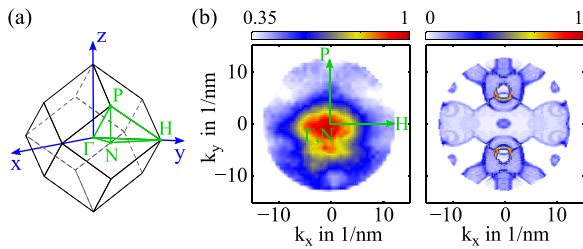


FIG. 6. (a) Brillouin zone of the BCC lattice with symmetry points. (b) Measured k-space image from the valence band of tungsten employing broadband high harmonic EUV radiation (left) and the projection of a calculated Fermi surface (using an energy slice with a width of 200 meV) using the linear muffin tin orbital method (right). The measurement indicates the expected symmetry along the  $\Gamma$ -P and  $\Gamma$ -H direction. The color bar indicates the normalized signal intensity.

spectrometer occur probabilistically, special effort has been put into the synchronization of the data streams from the delay-line detector and the stereo ATI phase-meter in order to ensure a proper assignment between the recorded events from both devices. The resultant photoemission spectra as a function of the CEP are shown in Fig. 7. For this plot, an initial CEP binning of  $10^\circ$  is chosen which is interpolated to a bin width of  $5^\circ$  for a smoother appearance.

A pronounced modulation of the photoelectron signal as a function of the CEP is observed, see Fig. 7(b), where the modulation strength, which is about 50%, is illustrated by the black curve. The modulation periodicity of  $180^\circ$  indicates the inversion symmetry of the photoemission signal with respect to the NIR field. As the link between the photoemission process and the CEP of the NIR laser field is the HHG process, it is intuitive that the observed modulation constitutes a direct imprint of the CEP-dependent high harmonic yield, which is confirmed by a CEP-resolved HHG simulation, see Fig. 7(c).

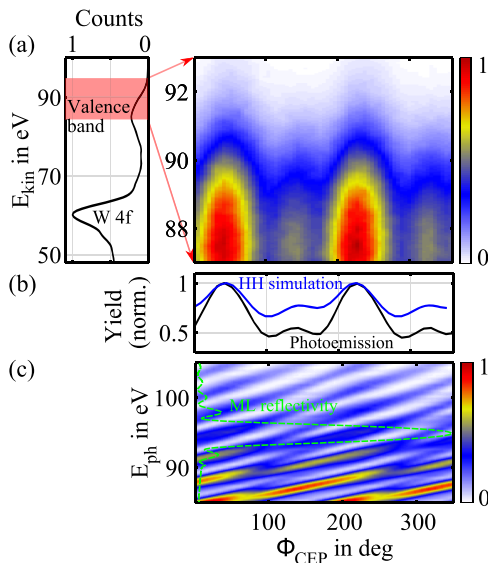


FIG. 7. (a) CEP-resolved photoemission spectra of the valence band of W(110) at 95 eV excitation energy. (b) Energy-integrated photoemission (measured, black) and high harmonic (simulated, blue) signal. A CEP-dependent periodic modulation in both signals is evident. The CEP dependency of the harmonic yield resembles the modulation behavior of the photoemission signal. (c) CEP-dependent high harmonic simulation. The dashed, green line indicates the spectral reflectivity of the multilayer (ML) mirror. The color bars indicate the normalized signal intensity.

The simulation code uses the applied laser pulse and gas target parameters and calculates the spatially coherent high harmonic response along the NIR beam profile at a single z-slice (where z is the propagation direction) using the Lewenstein model,<sup>45</sup> considering transient gas ionization. The contribution of long-trajectories is programmatically suppressed (by limiting the excursion time) as the same is also achieved by phase-matching adjustments in the experiment. Propagation effects, however, are not accounted for in order to limit the calculation time. The result shows the typical inclination of the spectral HH structure with respect to the CEP of the NIR field near the cutoff region.<sup>26,46</sup> The resultant CEP-dependent HH yield, derived by multiplying the simulated spectrum with the spectral reflectivity of the multilayer mirror and integrating it, is in good qualitative agreement with the measured modulation of the photoemission signal. A possible reason for the deviation in the modulation depth could be due to neglecting propagation effects in the simulation. Also, note that the ATI phase-meter only provides relative CE phases, i.e., the CEP axis of the photoemission signal,  $\Phi_{\text{CEP}}^{\text{PES}}$ , is only determined except for a constant offset, so that  $\Phi_{\text{CEP}}^{\text{PES}} = \Phi_{\text{CEP}} + \Phi_{\text{CEP}}^{\text{Offset}}$ , where  $\Phi_{\text{CEP}}$  is the real CEP referenced to a cosine pulse. The simulation can be used to estimate  $\Phi_{\text{CEP}}^{\text{Offset}}$ , which is close to zero in this case by coincidence.

#### IV. SUMMARY AND PROSPECTS

In this work, we have presented a new high harmonic beamline based on multi-pass amplifier technology with an increased repetition rate of 10 kHz. In spite of the reduced pulse energy compared to systems with lower repetition rate, we are able to generate harmonic output well beyond 100 eV with feasible flux for photoemission spectroscopy experiments. The HHG process is driven by 5 fs few-cycle pulses which form a spectral continuum in the high-energy part of the harmonic spectrum with a cutoff energy around 140 eV. Therefore, both electronic valence band states and core-like states can be addressed by this high harmonic radiation. Specially tailored EUV multilayer optics<sup>47</sup> are in use for steering, characterizing, and filtering the harmonic beam. By engineering the characteristics of the multilayer reflector in the main chamber, the beam parameters can be adapted to different experimental requirements. Broadband imaging of energy bands is required to sample band structure dynamics in the few-fs or even sub-fs time range. A k-space image of the valence band of tungsten, obtained by broadband high harmonic EUV excitation, is presented as an exemplary test case and reveals the expected symmetry of the lattice. Furthermore, the successful synchronization of the PES electron detector and the CE phase-meter is demonstrated by a CEP-resolved photoemission measurement on a tungsten (110) surface revealing a prominent CEP dependence in the photoelectron signal, which in turn reflects the CEP-dependent high harmonic yield near the cutoff. The conception of this measurement setup, i.e., single-shot CEP-tagging in combination with an angle-resolving time-of-flight electron spectrometer, enables a fast and efficient data acquisition as none of the parameters have to be scanned manually. CEP tagging also allows the selection of EUV pulses of different temporal structures arising from the varying CEP of

the driving pulse during the HHG process. In this way, the currently installed multilayer mirror in principle supports isolated sub-fs EUV pulses, extracted from the spectral harmonic continuum by amplitude gating, for ultimate time resolution in time-resolved photoemission experiments. The photoelectrons are recorded angle-resolved, and the spectrometer's performance regarding energy and angle resolution is characterized. It was found that the performance is currently limited by a poor electronic time resolution of the delay-line detector, which is about a factor of three above the common value for such a detector. Hence, an improvement of the spectrometer's performance can be expected regarding this issue. The experimental chamber is kept at UHV conditions and contains the tools necessary for sample handling, cleaning, and characterization.

We have proven the applicability of a 10 kHz high harmonic radiation and measurement infrastructure which is able to simultaneously capture a complete set of all the relevant parameters of few-cycle driven NIR pump–EUV probe photoemission experiments for the investigation of ultrafast band structure dynamics in solids. Important possible applications include, for instance, angle- and CEP resolved photoelectron streaking measurements at different binding energy levels from solid surfaces. The usage of recently developed EUV wave plates<sup>34</sup> even offers the potential to address electrons' spin-selectively, making this beamline an extremely versatile tool for ultrafast CEP-resolved studies of electron dynamics including magnetic and chiral materials.

## ACKNOWLEDGMENTS

This work was supported by the Deutsche Forschungsgemeinschaft (DFG) by the Excellence Cluster *Munich-Center for Advanced Photonics* (MAP).

<sup>1</sup>M. Hentschel, R. Kienberger, Ch. Spielmann, G. A. Reider, N. Milosevic, T. Brabec, P. Corkum, U. Heinzmann, M. Drescher, and F. Krausz, *Nature* **414**, 509–513 (2001).  
<sup>2</sup>M. F. Kling and M. J. J. Vrakking, *Annu. Rev. Phys. Chem.* **59**, 463–492 (2008).  
<sup>3</sup>E. Goulielmakis, V. S. Yakovlev, A. L. Cavalieri, M. Uiberacker, V. Pervak, A. Apolonski, R. Kienberger, U. Kleineberg, and F. Krausz, *Science* **317**, 769–775 (2007).  
<sup>4</sup>M. Schultze, M. Fieß, N. Karpowicz, J. Gagnon, M. Korbman, M. Hofstetter, S. Neppl, A. L. Cavalieri, Y. Komninos, Th. Mercouris, C. A. Nicolaides, R. Pazourek, S. Nagele, J. Feist, J. Burgdörfer, A. M. Azzeer, R. Ernstorfer, R. Kienberger, U. Kleineberg, E. Goulielmakis, F. Krausz, and V. S. Yakovlev, *Science* **328**, 1658–1662 (2010).  
<sup>5</sup>S. Neppl, R. Ernstorfer, A. L. Cavalieri, C. Lemell, G. Wachter, E. Magerl, E. M. Bothschafter, M. Jobst, M. Hofstetter, U. Kleineberg, J. V. Barth, D. Menzel, J. Burgdörfer, P. Feulner, F. Krausz, and R. Kienberger, *Nature* **517**, 342–346 (2015).  
<sup>6</sup>M. Wieland, Ch. Spielmann, U. Kleineberg, Th. Westerwalbesloh, U. Heinzmann, and T. Wilheina, *Ultramicroscopy* **102**, 93–100 (2005).  
<sup>7</sup>M. D. Seaberg, D. E. Adams, E. L. Townsend, D. A. Raymondson, W. F. Schlotter, Y. Liu, C. S. Menoni, L. Rong, C.-C. Chen, J. Miao, H. C. Kapteyn, and M. M. Murnane, *Opt. Express* **19**, 22470–22479 (2011).  
<sup>8</sup>A. Guggenmos, M. Jobst, M. Ossianer, S. Radünz, J. Riemensberger, M. Schäffer, A. Akil, C. Jakubeit, P. Böhm, S. Noever, B. Nickel, R. Kienberger, and U. Kleineberg, *Opt. Lett.* **40**, 2846–2849 (2015).  
<sup>9</sup>F. W. Helbing, G. Steinmeyer, J. Stenger, H. R. Telle, and U. Keller, *Appl. Phys. B* **74**, S35–S42 (2002).  
<sup>10</sup>J. Rauschenberger, T. Fuji, M. Hentschel, A.-J. Verhoef, T. Udem, C. Gohle, T. W. Hänsch, and F. Krausz, *Laser Phys. Lett.* **3**, 37–42 (2006).  
<sup>11</sup>E. Moon, H. Wang, S. Gilbertson, H. Mashiko, M. Chini, and Z. Chang, *Laser Photonics Rev.* **4**, 160–177 (2010).

<sup>12</sup>T. Wittmann, B. Horvath, W. Helml, M. G. Schätzel, X. Gu, A. L. Cavalieri, G. G. Paulus, and R. Kienberger, *Nat. Phys.* **5**, 357–362 (2009).  
<sup>13</sup>T. Rathje, N. G. Johnson, M. Möller, F. Süßmann, D. Adolph, M. Kübel, R. Kienberger, M. F. Kling, G. G. Paulus, and A. M. Saylor, *J. Phys. B: At., Mol. Opt. Phys.* **45**, 074003 (2012).  
<sup>14</sup>A. S. Alnaser, M. Kübel, R. Siemering, B. Bergues, N. G. Kling, K. J. Betsch, Y. Deng, J. Schmidt, Z. A. Alahmed, A. M. Azzeer, J. Ullrich, I. Ben-Itzhak, R. Moshhammer, U. Kleineberg, F. Krausz, R. de Vivie-Riedle, and M. F. Kling, *Nat. Commun.* **5**, 3800 (2014).  
<sup>15</sup>M. Kübel, N. G. Kling, K. J. Betsch, N. Camus, A. Kaldun, U. Kleineberg, I. Ben-Itzhak, R. R. Jones, G. G. Paulus, T. Pfeifer, J. Ullrich, R. Moshhammer, M. F. Kling, and B. Bergues, *Phys. Rev. A* **88**, 023418 (2013).  
<sup>16</sup>M. Krüger, S. Thomas, M. Förster, and J. Peter Hommelhoff, *J. Phys. B: At., Mol. Opt. Phys.* **47**, 124022 (2014).  
<sup>17</sup>P. B. Corkum, *Phys. Rev. Lett.* **71**, 1994 (1993).  
<sup>18</sup>E. J. Takahashi, T. Kanai, K. L. Ishikawa, Y. Nabekawa, and K. Midorikawa, *Phys. Rev. Lett.* **101**, 253901 (2008).  
<sup>19</sup>T. Popmintchev, M.-C. Chen, D. Popmintchev, P. Arpin, S. Brown, S. Ališauskas, G. Andriukaitis, T. Balčiunas, O. D. Mücke, A. Pugzlys, A. Baltuška, B. Shim, S. E. Schrauth, A. Gaeta, C. Hernández-García, L. Plaja, A. Becker, A. Jaron-Becker, M. M. Murnane, and H. C. Kapteyn, *Science* **336**, 1287–1291 (2012).  
<sup>20</sup>P. Rudawski, C. M. Heyl, F. Brizuela, J. Schwenke, A. Persson, E. Mansten, R. Rakowski, L. Rading, F. Campi, B. Kim, P. Johnsson, and A. L'Huillier, *Rev. Sci. Instrum.* **84**, 073103 (2013).  
<sup>21</sup>A. L. Cavalieri, N. Müller, Th. Uphues, V. S. Yakovlev, A. Baltuska, B. Horvath, B. Schmidt, L. Blümel, R. Holzwarth, S. Hendel, M. Drescher, U. Kleineberg, P. M. Echenique, R. Kienberger, F. Krausz, and U. Heinzmann, *Nature* **449**, 1029–1032 (2007).  
<sup>22</sup>M. Fieß, M. Schultze, E. Goulielmakis, B. Dennhardt, J. Gagnon, M. Hofstetter, R. Kienberger, and F. Krausz, *Rev. Sci. Instrum.* **81**, 093103 (2010).  
<sup>23</sup>E. Magerl, S. Neppl, A. L. Cavalieri, E. M. Bothschafter, M. Stanislawski, Th. Uphues, M. Hofstetter, U. Kleineberg, J. V. Barth, D. Menzel, F. Krausz, R. Ernstorfer, R. Kienberger, and P. Feulner, *Rev. Sci. Instrum.* **82**, 063104 (2011).  
<sup>24</sup>A. L. Cavalieri, E. Goulielmakis, B. Horvath, W. Helml, M. Schultze, M. Fieß, V. Pervak, L. Veisz, V. S. Yakovlev, and M. Uiberacker, *New J. Phys.* **9**, 242 (2007).  
<sup>25</sup>S. Hädrich, A. Klenke, J. Rothhardt, M. Krebs, A. Hoffmann, O. Pronin, V. Pervak, J. Limpert, and A. Tünnemann, *Nat. Photonics* **8**, 779–783 (2014).  
<sup>26</sup>P. Rudawski, A. Harth, C. Guo, E. Lorek, M. Miranda, C. M. Heyl, E. W. Larsen, J. Ahrens, O. Prochnow, T. Binhammer, U. Morgner, J. Mauritsson, A. L'Huillier, and C. L. Arnold, *Eur. Phys. J. D* **69**, 70 (2015).  
<sup>27</sup>I. Pupeza, S. Holzberger, T. Eidam, H. Carstens, D. Esser, J. Weitenberg, P. Rußbüldt, J. Rauschenberger, J. Limpert, Th. Udem, A. Tünnemann, T. W. Hänsch, A. Apolonski, F. Krausz, and E. Fill, *Nat. Photonics* **7**, 608–612 (2013).  
<sup>28</sup>C.-T. Chiang, A. Blättermann, M. Huth, J. Kirschner, and W. Widdra, *Appl. Phys. Lett.* **101**, 071116 (2012).  
<sup>29</sup>M. Chini, K. Zhao, and Z. Chang, *Nat. Photonics* **8**, 178–186 (2014).  
<sup>30</sup>A. M. Saylor, T. Rathje, W. Müller, K. Rühle, R. Kienberger, and G. G. Paulus, *Opt. Lett.* **36**, 1–3 (2011).  
<sup>31</sup>M. Hofstetter, M. Schultze, M. Fieß, B. Dennhardt, A. Guggenmos, J. Gagnon, V. Yakovlev, E. Goulielmakis, R. Kienberger, E. M. Gullikson, F. Krausz, and U. Kleineberg, *Opt. Express* **19**, 1767–1776 (2011).  
<sup>32</sup>M. Hofstetter, A. Aquila, M. Schultze, A. Guggenmos, S. Yang, E. Gullikson, M. Huth, B. Nickel, J. Gagnon, V. S. Yakovlev, E. Goulielmakis, F. Krausz, and U. Kleineberg, *New J. Phys.* **13**, 063038 (2011).  
<sup>33</sup>A. Guggenmos, R. Rauhut, M. Hofstetter, S. Hertrich, B. Nickel, J. Schmidt, E. M. Gullikson, M. Seibald, W. Schnick, and U. Kleineberg, *Opt. Express* **21**, 21728–21740 (2013).  
<sup>34</sup>J. Schmidt, A. Guggenmos, M. Hofstetter, S. H. Chew, and U. Kleineberg, *Opt. Express* **23**, 33564–33578 (2015).  
<sup>35</sup>S. H. Chew, A. Gliserin, J. Schmidt, H. Bian, S. Nobis, F. Schertz, M. Kübel, Y.-Y. Yang, B. Loitsch, T. Stettner, J. J. Finley, C. Späth, H. Ouacha, A. M. Azzeer, and U. Kleineberg, *Appl. Phys. B* **122**, 102 (2016).  
<sup>36</sup>S. H. Chew, F. Süßmann, C. Späth, A. Wirth, J. Schmidt, S. Zherebtsov, A. Guggenmos, A. Oelsner, N. Weber, J. Kapaldo, A. Gliserin, M. I. Stockman, M. F. Kling, and U. Kleineberg, *Appl. Phys. Lett.* **100**, 051904 (2012).  
<sup>37</sup>R. K. Nubling and J. A. Harrington, *Opt. Eng.* **37**, 2454–2458 (1998).

- <sup>38</sup>V. Pervak, I. Ahmad, M. K. Trubetskov, A. V. Tikhonravov, and F. Krausz, *Opt. Express* **17**, 7943 (2009).
- <sup>39</sup>A. M. Sayler, T. Rathje, W. Müller, Ch. Kürbis, K. Rühle, G. Stibenz, and G. G. Paulus, *Opt. Express* **19**, 4464–4471 (2011).
- <sup>40</sup>T. Popmintchev, M.-C. Chen, A. Bahabad, M. Gerrity, P. Sidorenko, O. Cohen, I. P. Christov, M. M. Murnane, and H. C. Kapteyna, *Proc. Natl. Acad. Sci. U. S. A.* **106**, 10516–10521 (2009).
- <sup>41</sup>K. S. Budil, P. Salières, A. L'Huillier, T. Ditmire, and M. D. Perry, "Influence of ellipticity on harmonic generation," *Phys. Rev. A* **48**, R3437 (1993).
- <sup>42</sup>A. Oelsner, M. Rohmer, Ch. Schneider, D. Bayer, G. Schönhense, and M. Aeschlimann, *J. Electron Spectrosc. Relat. Phenom.* **178**, 317–330 (2010).
- <sup>43</sup>A. Baltuska, M. Uiberacker, E. Goulielmakis, R. Kienberger, V. S. Yakovlev, T. Udem, T. W. Hansch, and F. Krausz, *IEEE J. Sel. Top. Quantum Electron.* **9**, 972–989 (2003).
- <sup>44</sup>Kh. Zakeri, T. R. F. Peixoto, Y. Zhang, J. Prokop, and J. Kirschner, *Surf. Sci.* **604**, L1–L3 (2010).
- <sup>45</sup>M. Lewenstein, Ph. Balcou, M. Yu. Ivanov, A. L'Huillier, and P. B. Corkum, *Phys. Rev. A* **49**, 2117 (1994).
- <sup>46</sup>M. Krebs, S. Hädrich, S. Demmler, J. Rothhardt, A. Zaïr, L. Chipperfield, J. Limper, and A. Tünnermann, *Nat. Photonics* **7**, 555–559 (2013).
- <sup>47</sup>A. Guggenmos, S. Radünz, R. Rauhut, M. Hofstetter, S. Venkatesan, A. Wochnik, E. M. Gullikson, S. Fischer, B. Nickel, C. Scheu, and U. Kleineberg, *Opt. Express* **22**, 26526–26536 (2014).